Coupling of Epsilon-Near-Zero Mode to Mushroom-Type Metamaterial for Optimizing Infrared Suppression and Radiative Cooling

Jiacheng LI[1], Shuang LIU[1*], Shenglan WU[1], Yong LIU[1], and Zhiyong ZHONG[2]

[1]*State Key Laboratory of Electronic Thin Films and Integrated Devices, School of Optoelectronic Science and Engineering, University of Electronic Science and Technology of China, Chengdu 611731, China*

[2]*School of Electronic Science and Engineering, University of Electronic Science and Technology of China, Chengdu 611731, China*

[*]Corresponding author: Shuang LIU E-mail: shuangliu@uestc.edu.cn

Abstract: We report a complementary metal oxide semiconductor (CMOS) compatible metamaterial-based spectrally selective absorber/emitter (MBSSAE) for infrared (IR) stealth, which has the low absorption/emissivity in the IR atmospheric transmission window (3 μm – 5 μm, 8 μm – 14 μm) and ultra-high and broadband absorption/emissivity in the IR non-atmospheric window (5 μm – 8 μm). We propose a novel method for the broadband absorption/emissivity in 5 μm – 8 μm with incorporation of an epsilon-near-zero (ENZ) material between the top patterned aluminum (Al) disks layer and the silicon oxide (SiO_2) spacer layer. With an appropriate design, the peaks in the IR atmospheric transmission window can be suppressed while the peak intensity in the non-atmospheric window remains high. The optimized MBSSAE has an average absorption/emissivity less than 10% in 8 μm – 14 μm and less than 6% in 3 μm – 5 μm. And the average absorption/emissivity in 5 μm – 8 μm is approximately over 64%. This proposed scheme may introduce the opportunities for the large-area and low-cost infrared stealth coating, as well as for the radiative cooling, spectral selective thermal detector, optical sensor, and thermophotovoltaic applications.

Keywords: Metamaterials; infrared stealth; ENZ mode; Rabi splitting; broadband thermal emitter

Citation: Jiacheng LI, Shuang LIU, Shenglan WU, Yong LIU, and Zhiyong ZHONG, "Coupling of Epsilon-Near-Zero Mode to Mushroom-Type Metamaterial for Optimizing Infrared Suppression and Radiative Cooling," *Photonic Sensors*, 2023, 13(2): 230231.

1. Introduction

Stealth is an essential anti-reconnaissance technique to effectively blend objects into ambient environments and minimize the possibility of being detected. Based on the passive detection mechanism of the infrared imaging, dynamically controlling infrared radiative features of the object is critical in infrared stealth. According to the Stefan-Boltzmann law, the radiative power is related to the surface temperature and the emissivity of the objects. Thus, the focus of the past research in infrared stealth mostly was to control the temperature of the objects, and controlling the infrared emittance of objects is an alternative scheme for the stealth in the infrared spectrum [1–6]. Recently, the dynamical control of the thermal emission for adaptive infrared stealth has attracted extensive research interests [5, 7, 8]. There has been considerable progress in the spectrum, directionality, polarization, and temporal

Received: 6 July 2022 / Revised: 30 September 2022

DOI: 10.1007/s13320-022-0672-7
Article type: Regular

response of thermal emitter using varied nanostructured materials, e.g., dielectric gratings [9, 10], photonic crystals [11–13], metamaterials/ metasurfaces [14–19], and multilayer films [20, 21].

For the infrared stealth application, most materials have the low emissivity over the entire infrared range and may increase the risk of being detected to some extent due to the gradually accumulated energy [21]. This problem can be effectively solved by utilizing the concept of radiative cooling, that is, the non-atmospheric window acts as a channel for the heat dissipation to design a wavelength-selective emitter with the high emissivity in the non-atmospheric window (5 μm – 8 μm) and low emissivity in the atmospheric window (3 μm – 5 μm and 8 μm – 14 μm). Wavelength-selective thermal radiation is required for the ideal infrared stealth materials in order to avoid the accumulated energy risk and mitigate the thermal instability [1, 4, 22–24].

Metamaterials are artificially constructed materials, which consist of either periodic or random arrays of subwavelength elements (meta-atoms) whose spatially averaged response can be treated as that of an effective homogeneous medium with an effective permittivity (ε) and permeability (μ). This permits the optical properties of the metamaterials to be engineered deliberately. Such unusual properties of the metamaterials have enabled exciting applications such as perfect lenses [25] and electromagnetic invisibility cloaks [26]. Another important application of the metamaterials is the development of the perfect absorber, in which the metamaterials can result in near unity absorbance/ emittance over a desired frequency range (that is, spectrally selective perfect absorption/emissivity) [27–30]. This enables the metamaterials to offer more freedom degrees to tune the infrared radiative properties of targets, thus, a suitable candidate for satisfying the requirements of an ideal infrared stealth material.

The metamaterial perfect absorber was first demonstrated by Landy *et al.* [27] at microwave frequencies using a combination of split-ring resonators (SRRs) and cut wire pairs to tune the electric and magnetic responses independently. Efforts to demonstrate the metamaterial spectral perfect absorber/emitter in the infrared have converged on a theme of simplified designs that essentially consist of a sub-wavelength-scale resonator separated from an optically thick metal film by an intermediate dielectric layer [1, 4, 14, 15, 30–34].

However, unexpected resonances in metamaterial-based selective emitters could lead to exposure to the infrared dual-band detection systems. As shown in Fig. 1, the metamaterial-based selective emitter exhibits two absorption/emissivity peaks, and the peak lies in the band of 8 μm –14 μm could lead to degrading stealth performance. In this paper, we characterize the two absorption/emissivity peaks and figure out the origins of the two peaks. And then, we propose an optimized metamaterial-based spectrally selective absorber/emitter (MBSSAE) with incorporation of an epsilon-near-zero (ENZ) material between the patterned Al disks and the SiO_2 spacer layer. We show that the coupling of the magnetic polaritons to the ENZ mode [35, 36] can significantly broaden the absorption/emissivity in the band of 5 μm –8 μm. The optimized selective emitter can effectively suppress the thermal radiation in the two atmospheric windows and enhance the thermal radiation in the non-atmospheric window. The results of this study will contribute to a further understanding of the metamaterials for multi-resonance and mode coupling behavior, which enables further ideas for designing the narrow-band or broadband absorber/ emitter.

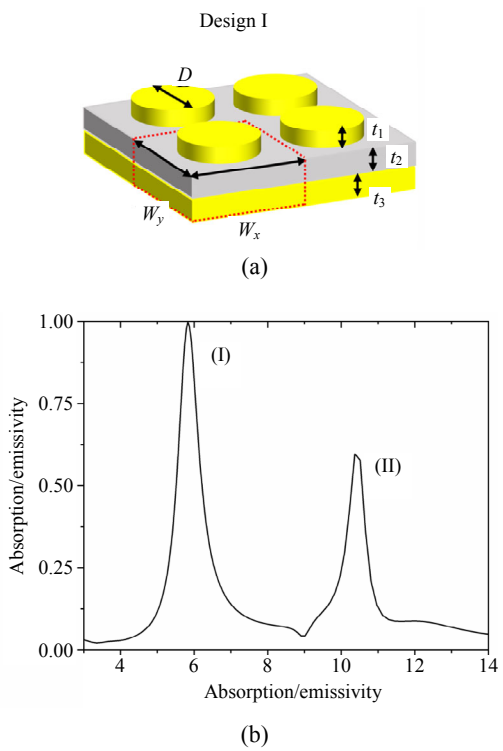

Fig. 1 Prototype-design of MBSSAE structures: (a) three-dimensional (3D) schematic of the first designed (Design I) MBSSAE (the yellow patterns represent Al, and the grey patterns represent SiO_2) and (b) simulated absorption spectra of the MBSSAEs. The geometric parameters of (a) are t_1 = 50 nm, t_2 = t_3 = 100 nm, W_x = W_y = 2.6 μm, and D = 2.2 μm. The two absorption band peaks are labelled as I and II.

2. Numerical simulation method

To investigate the performance of our design numerically, we employ a commercial software package [lumerical finite difference time domain (FDTD)] [37] by utilizing the FDTD method. The schematic of the metamaterial-based spectrally selective absorber/emitter for infrared stealth is shown in Fig. 1(a), which consists of a patterned array of the Al disks and a layer of the Al film separated by a layer of SiO_2. In the simulations, complex optical constants for SiO_2 are taken from [38], and the optical properties for Al are taken from [39]. We select highly doped silicon (Si) as the ENZ material in the mid infrared (MIR), and the dielectric constant of doped silicon is described by a Drude model, as shown below:

$$\varepsilon_{\mathrm{Si}}(\omega)=\varepsilon_{\infty}-\frac{\omega_p^2}{\omega^2+\mathrm{i}\omega\gamma} \tag{1}$$

where ε_∞ (= 11.7) is the permittivity of doped silicon at the high frequency, and ω_p is the plasma frequency [$\omega_p^2=n_d e^2/(\varepsilon_0 m_{\mathrm{eff}})$], in which n_d is the doping density, m_{eff} is the effective mass of the carriers, e is the charge on an electron, ε_0 is the permittivity of the vacuum), and γ is the collision frequency [$\gamma=e/(m_{\mathrm{eff}}\mu_c)$], where μ_c is the mobility of the carriers).

The simulation region geometry is symmetrical in the *xy*-plane, so the boundary condition is chosen to be symmetric along the *y*-axis and anti-symmetric along the *x*-axis for faster simulation. The boundary condition along the *z*-direction is taken as a perfect matched layer (PML). The minimum mesh step is 10 nm, and a mesh accuracy of 2 is taken. The simulation time is taken as 3000 fs. We calculate the absorptivity (A) as follows: $A = 1-R-T$, where R is the reflectivity, and T is the transmittance. According to Kirchhoff's law, the absorptivity is equal to the emissivity [40]. We can therefore determine the emissivity from the simulated absorptivity results. The thickness of the Al ground plane is larger than the skin depth of electromagnetic waves in the infrared regime and will block any light transmitted, leading to nearly zero transmittivity in the range of the interest. In the following simulation and discussion, the transmittivity is set to zero, and we calculate the absorptivity (A) as follows: $A = 1-R$.

3. Results and discussion

3.1 Mechanism and prototype design

Our prototype-design of MBSSAE structures consists of a three-layer system as follows: a layer of SiO_2 is sandwiched between an optically thick layer of Al and a patterned layer of the square periodic array of Al disks, as shown in Fig. 1(a).

The Al disk on the top acts as electric resonators driven by the electric field of the incident radiation [30]. And a magnetic resonance can be excited by

the antiparallel surface currents in the top Al disk and the Al ground plane. These two antiparallel currents act to form circulating current loops with a confined magnetic field. The induced circulating currents result in a magnetic dipole [30] moment which can strongly interact with the magnetic field of the incident radiation.

A change in the top Al disk diameter will result in a shift of the electric resonance frequency and hence, result in a change of the effective dielectric permittivity $\varepsilon(\omega)$ of the system. In comparison, a change in the SiO_2 layer thickness primarily affects the magnetic resonance and will control the effective magnetic permeability $\mu(\omega)$ of the system. The capacitive coupling to the Al ground plane will also contribute to $\varepsilon(\omega)$, but to a lesser extent. When tuning the electric and magnetic resonance frequencies, their relative strengths can give rise to an optimal impedance matching for the incident radiation. Thus, the combination of the optimized diameter of the Al disk and the thickness of the SiO_2 spacer layer enables the impedance to match with the incident medium, thereby, giving rise to the perfect absorption of the radiation [28].

An early research [33] demonstrated that the primary resonance may rise from a localized surface plasmon, and we can consider such structure as a metal-insulator-metal (MIM) configuration where two semi-infinite slabs of the metal are separated by a thin and planar dielectric layer with the thickness of t_2, and solve the dispersion relation for a transverse magnetic plasmon polariton. The primary resonance of a circular patch is then given by

$$\lambda = \frac{\pi D}{1.841} n_d \left(1 + \frac{2c}{\omega_p t_2}\right)^{1/2}. \quad (2)$$

In (2), the primary resonant (or fundamental mode) wavelength is proportional to the diameter D of the top metal disk and the primary resonant (or fundamental mode) wavelength is also proportional to the optical index n_d of the intermediate dielectric layer. Equation (2) suggests a theoretical basis for designing the metamaterial-based absorber/emitter in the frequency of interest.

First in our prototype designed MBSSAE (Design I), the thickness of the top patterned Al layer is 50 nm (t_1 = 50 nm), the dielectric layer and bottom Al ground layer have the same thickness of 100 nm ($t_2 = t_3$ = 100 nm), the period/pitch of the unit cell is $W_x = W_y$ = 2.6 μm, and the diameter of the top Al disk is D = 2.2 μm, as shown in Fig. 1(a). The simulation result is represented as the black curve in Fig. 1(b). There are two absorption band peaks at 5.8 μm and 10.4 μm.

To understand the origins of the two resonance peaks shown in Fig. 1(b), we calculate the intensity of the magnetic and electric field distributions at different resonance wavelengths for Design I of the metamaterial-based absorber/emitter, as shown in Fig. 2. Figure 2(b) shows the magnetic field distribution in the unit cell at the wavelength of 5.8 μm (Peak I in Fig. 1b), representing the first-order magnetic resonance, and both the electric field [Fig. 2(a)] and the magnetic field [Fig. 2(b)] represent localized mode features. As shown in Fig. 2(d), the magnetic field in the unit cell at the wavelength of 10.4 μm [Peak II in Fig. 1(b)] represents the same localized field distribution features with the case at the wavelength of 5.8 μm, which is also corresponding to the first-order magnetic resonance.

The reason for the coexisting of these two first-order magnetic polariton resonances in such structure is attributed to the strong dispersion characteristic of SiO_2 in the range from 7 μm to 12 μm [as shown in Fig. 3(a)]. As shown in Fig. 3(b), Peaks I and II both redshift with an increase in the top Al disk diameter. Peak I gradually approaches the longitudinal optical (LO) phonon wavelength of SiO_2, while Peak II gradually deviates from the transverse optical (TO) phonon wavelength of SiO_2. Figure 3(c) depicts an anti-crossing behavior of the magnetic polariton resonance due to the coupling of the intrinsic material phonon resonance of SiO_2 and

the diameter-dependent magnetic polariton resonance. The wavelength at permittivity near zero is called the epsilon-near-zero (ENZ) wavelength (λ_{ENZ}), in which the ENZ mode can be excited. We can demonstrate that the strong coupling between the ENZ mode and magnetic polariton results in a significant Rabi splitting. Previous works have demonstrated similar results [41–43].

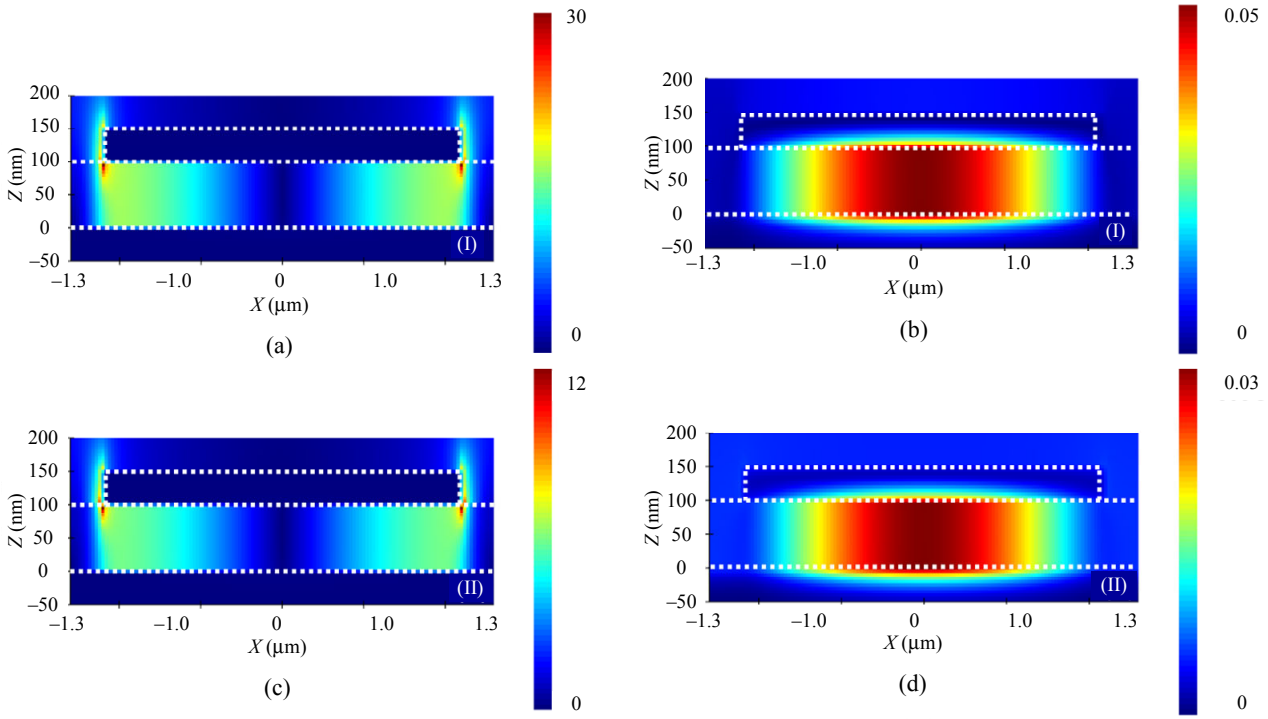

Fig. 2 Simulated spatial profiles of the electric field intensity for the first designed MBSSAE at the incident wavelength of (a) 5.8 μm and (c) 10.4 μm, respectively and simulated spatial profiles of the magnetic field intensity for the first designed MBSSAE at the incident wavelength of (b) 5.8 μm and (d) 10.4 μm, respectively.

To clarify the origin of the split absorption peaks, we perform a theoretical analysis of the coupled system, which can be written as [43]

$$\begin{pmatrix} \omega^2-\omega_{TO}^2 & \omega\omega_s \\ \omega\omega_s & \omega^2-\omega_{MP}^2 \end{pmatrix}\begin{pmatrix} \omega x \\ \sqrt{\varepsilon_\infty/4\pi}E \end{pmatrix}=0 \qquad (3)$$

and the permittivity of SiO_2 is written as

$$\begin{aligned}\varepsilon_{SiO_2} &= \varepsilon_\infty\left(1+\frac{\omega_{LO}^2-\omega_{TO}^2}{\omega_{TO}^2-\omega^2-i\gamma\omega}\right)\\ &= \varepsilon_\infty\left(1+\frac{\omega_s^2}{\omega_{TO}^2-\omega^2-i\gamma\omega}\right)\end{aligned} \qquad (4)$$

where E is the field amplitude, ω_{MP} is the magnetic polariton frequency, ω_{TO} is the TO phonon frequency, and ω_{LO} is the LO phonon frequency. Note that the simpler coupled-harmonic-oscillator model does not show the ω-dependence of the off-diagonal terms and therefore cannot describe the polaritonic branches correctly.

In the ultrastrong coupling (USC) regime at the crossing point of the magnetic resonant and TO phonon frequencies ($\omega_{MP} = \omega_{TO}$), as shown in Fig. 3(c), the exact frequencies of the two polaritonic branches are

$$\omega_\pm = \sqrt{\omega_{TO}^2+\frac{\omega_s^2}{4}} \pm \frac{\omega_s}{2}. \qquad (5)$$

And the splitting is calculated to be $\Delta\omega = |\omega_+ - \omega_-| = \omega_s$, the TO and LO phonon frequencies of SiO_2 are 32.24 THz and 36.4 THz, respectively, through which the value of ω_s is calculated to be 16.9 THz. From Fig. 3(c), the coupling strength g (= $\Delta\omega/2$) is approximately 8.5 THz, which is consistent with the

half value of ω_s. Moreover, the normalized coupling strength (η) is calculated by $\eta = g/\omega_{TO} \approx 0.264 >$ 0.25, indicating that the systems are in the ultrastrong coupling regime [43].

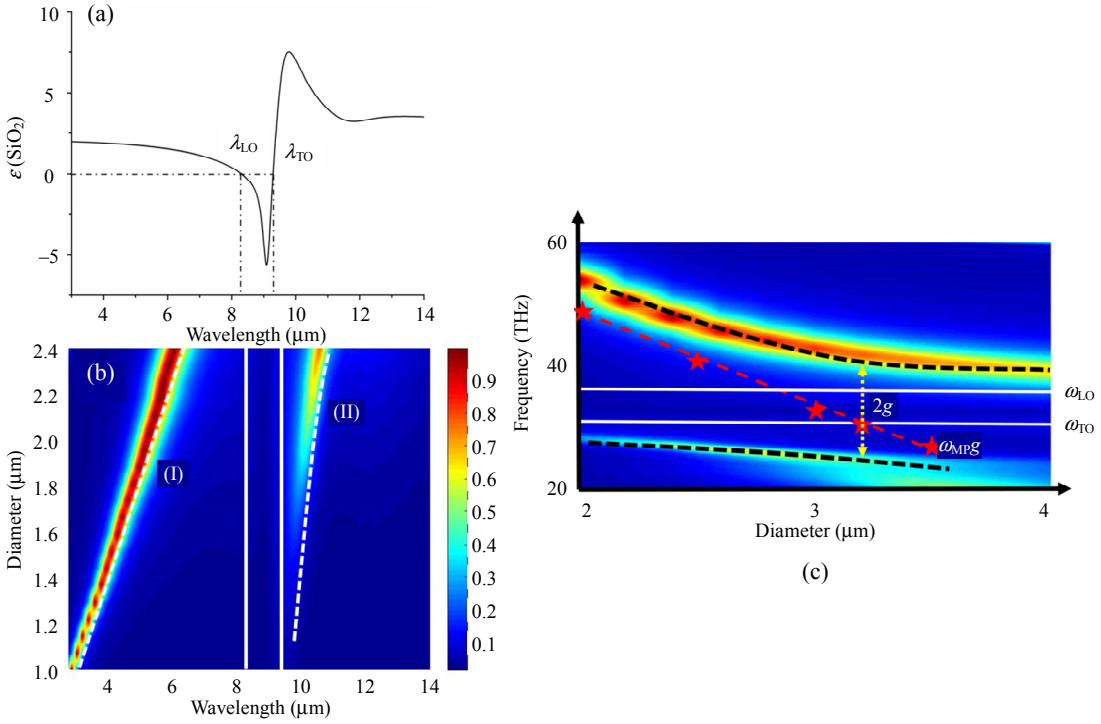

Fig. 3 Coupling of the intrinsic material phonon resonance of SiO_2 and the magnetic polariton resonance: (a) real part of the permittivity of SiO_2 as a function of the wavelength, (b) simulated absorbance of the first designed MBSSAE as a functions of the wavelength and the top Al disk diameter with other parameters t_1 = 50 nm, t_2 = t_3 = 100 nm, and W_x = W_y = 2.6 μm (the two vertical white solid lines indicate the locations of the LO and TO phonon wavelengths of SiO_2, respectively, and the white dashed lines represent the wavelength with the maximum absorption efficiency of the first designed MBSSAE), and (c) schematic illustration of the Rabi splitting (the red dashed line indicates the magnetic polariton mode, and the black dashed lines indicate the two polaritonic branches).

3.2 Optimization of the structural design

Based on the mode resonant mechanisms of the metamaterial-based absorber/emitter, we can further optimize the absorption/emission performance for the purpose of infrared stealth. The absorption spectra could be tuned by changing the diameter D of the disk. The dependence of absorption spectra on changes in the diameter of the disk is shown in Fig. 4(a). The significant changes in the absorption/emissivity intensity of Peak II are clearly shown in Figs. 4(b) and 4(c). Though the absorption intensity of Peak II is suppressed as a decrease in the Al disk diameter D, both Peaks I and II shift toward shorter wavelengths, which results in a lower emissivity in 5 μm – 8 μm and a much higher emissivity in 3 μm – 5 μm.

For further optimizing our structure, we then propose the second designed (Design II) MBSSAE, as shown in Fig. 5(a). Figure 5(c) shows the dependence of absorption spectra on the SiO_2 cylinder diameter D_s. As can be seen, both Peaks I and II have slightly blue-shifts with a decrease in the SiO_2 cylinder diameter, and Peak II is decreasing gradually and eventually totally disappears. This result can be explained with (6) as follows [34]:

$$\lambda_r = 2n_{\text{eff}}D \tag{6}$$

where n_{eff} is the effective index of the MIM waveguide, D is the diameter of the Al disk, and λ_r is the resonant wavelength. When the spacer layer is etched into an array of cylinder, the effective index

n_{eff} of the MIM waveguide slightly decreases, which results in the resonance wavelength shifts slightly to the shorter wavelength. Equation (6) can be thought of as a further simplification of (2), since the physical mechanism of the two formulas is consistent.

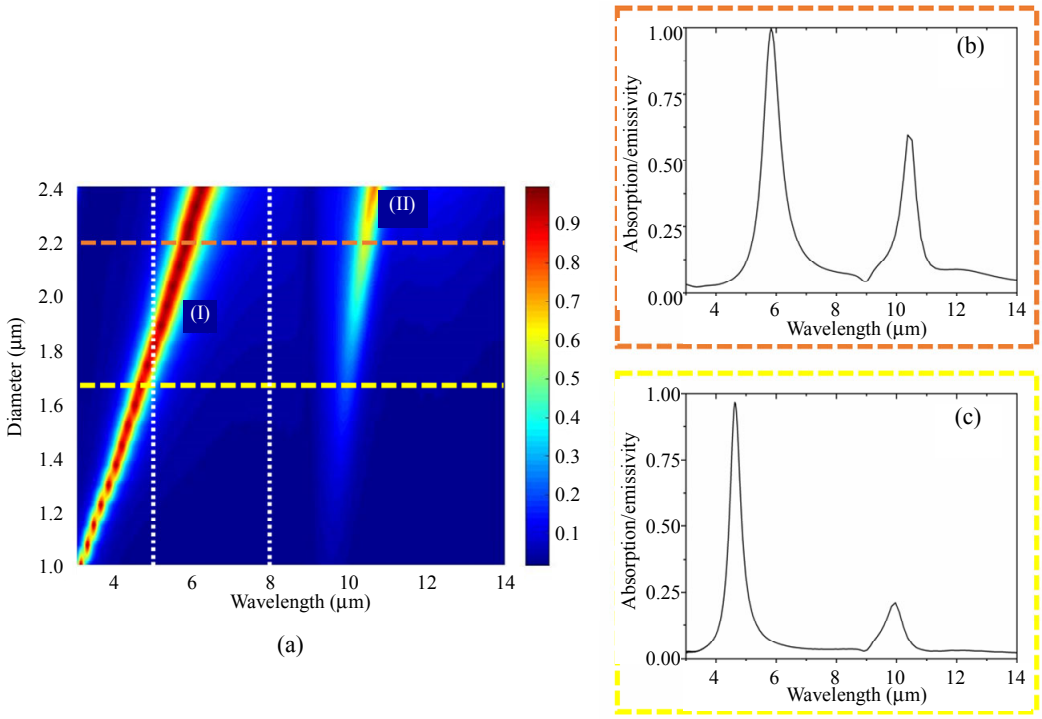

Fig. 4 Simulated absorbance of the first designed MBSSAE (a) as functions of the wavelength and the top Al disk diameter with other parameters t_1 = 50 nm, $t_2 = t_3$ = 100 nm, and $W_x = W_y$ = 2.6 μm. The white dashed line region corresponds to the non-atmospheric window (5 μm – 8 μm), the orange dashed line parallel to the x-axis represents the configuration with the disk diameter of D = 2.2 μm, and the corresponding spectrum is shown in (b), and the yellow dashed line parallel to the x-axis represents the configuration with the disk diameter of D = 1.66 μm, and the corresponding spectrum is shown in (c).

Considering the limitation of the fabrication condition, it is hard to achieve a perfect cylinder shape in the etching process of the dielectric layer, so we replace the SiO_2 cylinder with a circular truncated cone as the third design (Design III). We create the mushroom-capped structure [as illustrated in Fig. 5(b)] by additional fabrication processing: a predominately anisotropic reactive-ion-etching (RIE) or wet-etching with the slight isotropic component is carried out to remove the SiO_2-spacer laterally at a slower speed than that of etching downward. For those circular truncated cones with a relatively small tilt angle, we probably need the lateral etching rate faster than the longitudinal etching rate. The etched shape can be controlled by the etching time and the choices of etching gas or solution. As discussed above, the resonance wavelength is approximately proportional to the effective index n_{eff} and the diameter of the Al disk D. Based on the effective medium theory (EMT), in our second and third design cases, the effective index n_{eff} depends on the volume duty ratio of SiO_2. Here, we depict six different samples of the third designed MBSSAE, of which Samples (1) – (5) have the same volume duty ratio of the SiO_2 truncated cone, to make sure that the effective index n_{eff} is consistent with that of Design II. In addition, Sample (6) has a little smaller volume duty ratio of SiO_2 than else. The corresponding calculated values of D_t and D_b are listed in Table 1. The period, Al disk diameter, and spacer thickness are fixed as $W_x = W_y$ = 2.8 μm, D = 2.6 μm, and t_2 = 100 nm, respectively.

Table 1 Detailed geometric parameters of Designs II and III.

Sample	Design II	Design III					
		(1)	(2)	(3)	(4)	(5)	(6)
D_t (μm)	1.8	1.6	1.4	1.2	1	2.5	1
D_b (μm)	1.8	2	2.172	2.34	2.5	1	1.4
Volume duty ratio (%)	33	33	33	33	33	33	15
Tilt angle (°)	90	27	15	10	8	8	27

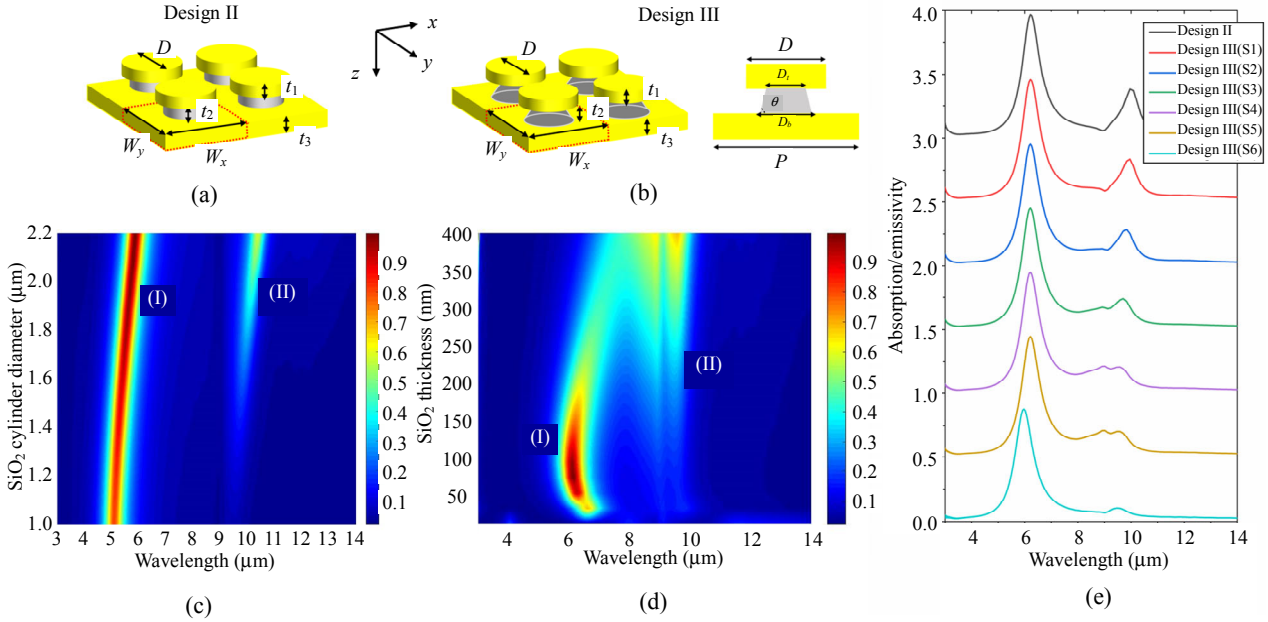

Fig. 5 Second and third design schemes of MBSSAE structures: (a) 3D schematic of the second designed MBSSAE, the spacer layer is etched to be an array of the cylinder with a smaller diameter D_s than that of the top Al disk, (b) left: 3D schematic of the third designed MBSSAE and right: cross-section of Design III, in which the SiO_2 spacer is etched to be an array of the circular truncated cone with a top diameter D_t and a bottom diameter D_b, (c) simulated absorption spectra of the second MBSSAEs as functions of the wavelength and the SiO_2 disk diameter D_s with other parameters t_1 = 50 nm, t_2 = t_3 = 100 nm, W_x = W_y = 2.6 μm, and D = 2.2 μm, (d) simulated absorption spectra of the third designed MBSSAEs as functions of the wavelength and the SiO_2 thickness t_2 with other parameters t_1 = 50 nm, t_3 = 100 nm, W_x = W_y = 2.8 μm, D = 2.6 μm, D_t = 1 μm, and D_b = 2.5 μm, and (e) calculated absorption spectra for Design II with D_s = 1.8 μm and Design III with varied values of D_t and D_b, other parameters are fixed as t_1 = 50 nm, t_2 = t_3 = 100 nm, W_x = W_y = 2.8 μm, and D = 2.6 μm. All the curves are shifted by 50% in the y-axis direction for clarity.

The simulated results are displayed in Fig. 5(e), for Samples (1) – (5), Peak I remains unchanged as the volume duty ratio of the SiO_2 truncated cone stays the same, and it is furtherly demonstrated from the spectral curve of Sample (6) that a slight blue-shift of Peak I is due to the changes in the volume duty ratio of SiO_2.

By contrast, Peak II is much more sensitive to the geometric parameters of the SiO_2 truncated cone. Here, we define the tilt angle θ as the angle between the hypotenuse and the long length of the truncated cone. Accordingly, the truncated cone in Sample (1) has a larger tilt angle, Sample (4) has a smaller tilt angle, and Sample (5) has an inverted truncated cone with a consistent tilt angle as that of the SiO_2 truncated cone from Sample (4). As can be seen from the curve of Sample (1) to that of Sample (4), Peak II is gradually suppressed and accompanied by a slight spectral blue-shift. As for the curve from Sample (5), the spectral curve is almost the same as that of Sample (4). As a result, the tilt angle θ of the truncated cone might be the key of the coupling

behavior between the metamaterial magnetic resonance and the SiO_2 phonon resonance.

Figure 5(d) depicts the dependence of the SiO_2 thickness on the absorption, there exists an optimized value of the SiO_2 thickness to meet the critical coupling condition for perfect absorption, and we select the optimized SiO_2 thickness to be t_2 = 100 nm.

As for the result from Sample (6), the calculated average absorption is approximately 5.7% in 8 μm – 14 μm and less than 5% in 3 μm – 5 μm. The average absorption in 5 μm – 8 μm remains 35.9% simultaneously, which is relatively low in the infrared stealth application.

Further efforts have been made to broaden the absorption bandwidth of 5 μm – 8 μm. We utilize doped silicon as the ENZ material with the plasma frequency tuned by the doped concentrations. We set the n-doped concentration to $N_n = 1.07 \times 10^{20}\,\mathrm{cm}^{-3}$. In our simulation, the dielectric constant of n-doped Si is described by the Drude model with a plasma frequency of $\omega_p = 1.12 \times 10^{15}$ rad/s and a collision frequency of $\gamma = 5 \times 10^{13}$ rad/s. The resulted ENZ wavelength of our designed n-doped Si is near the wavelength of λ = 6 μm. The n-doped Si nanolayer is integrated between the top patterned Al disks layer and the SiO_2 spacer layer, as shown in Fig. 6(a). Figure 6(b) shows that a nanofilm of n-doped Si can

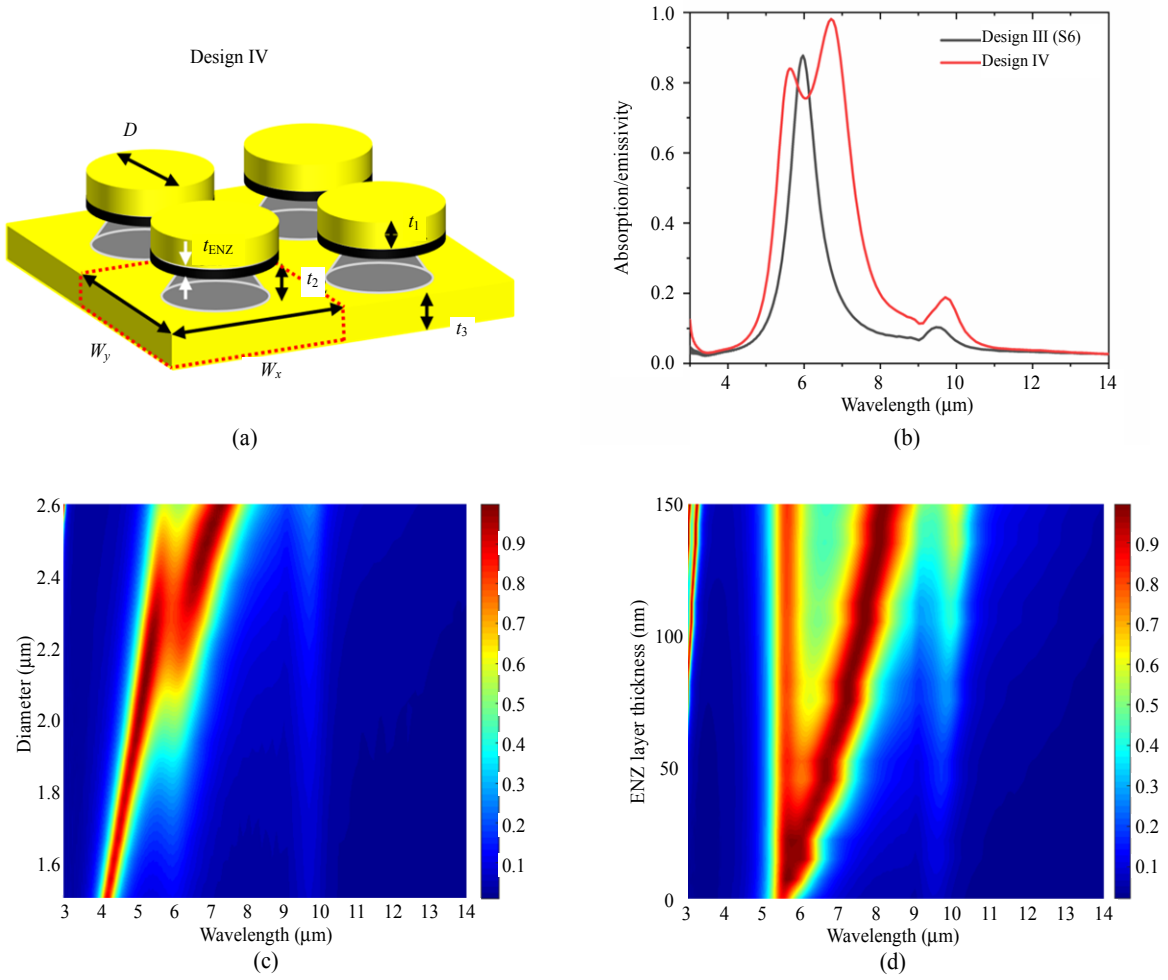

Fig. 6 Fourth design scheme of MBSSAE structures: (a) 3D schematic of the fourth design, (b) simulated absorption spectra of the MBSSAEs with different designs, in which the red and black curves represent the third designed MBSSAE and the fourth designed MBSSAE, respectively (the geometric parameters of Designs III and IV are listed in Table 2), (c) simulated absorption spectra with the change of the top Al disk diameter D (the other parameters are t_1 = 50 nm, $t_2 = t_3$ = 100 nm, t_{ENZ} = 80 nm, and $W_x = W_y$ = 2.6 μm), and (d) simulated absorption spectra with the change of the thickness of the ENZ nanolayer (the other parameters are t_1 = 50 nm, $t_2 = t_3$ = 100 nm, $W_x = W_y$ = 2.6 μm, and D = 2.1 μm).

significantly broaden the absorption band near the ENZ wavelength, which is attributed to the mode coupling of the ENZ mode and the magnetic polariton resonance [35, 36]. For the fourth designed (Design IV) MBSSAE, these simulations reveal that an average absorption of less than 10% is maintained over the 8 μm – 14 μm band and an average absorption of 6% over the 3 μm – 5 μm band. Two absorption peaks occur in the 5 μm – 8 μm band with an average absorption increased to 65.8%.

We also investigate the impact of deviations in the geometry caused by fabrication tolerances, and the results are displayed in Figs. 6(c) and 6(d). As shown in Fig. 6(c), the top Al disk diameter has a significant effect on Peak I, and as the top Al disk diameter increases, Peak I shifts toward longer wavelengths and splits into two peaks near the ENZ wavelength of n-doped silicon; Fig. 6(d) shows that the thickness of the ENZ nanofilm has significant effects on both Peaks I and II. When the ENZ nanolayer thickness is less than 100 nm, an increase in the ENZ nanolayer thickness results in a higher and broadband emissivity in the 5 μm – 8 μm band.

Table 2 Detailed geometric parameters of Sample (6) in Designs III, and IV.

	Design III (S6)	Design IV
t_1 (nm)	50	50
t_2 (nm)	100	100
t_3 (nm)	100	100
t_{ENZ} (nm)	/	50
D (μm)	2.6	2.4
W_x (= W_y) (μm)	2.8	2.8
D_t (μm)	1	1
D_b (μm)	1.4	1.4

Then, we consider the effect of non-uniform doping of n-doped silicon and build a physical model of a multilayer stacked structure to simulate the inhomogeneity of doping concentration distribution in n-doped silicon, as shown in Fig. 7(a), and the thickness of each layer is $t_{ENZ}/5$. As we assume that the doping concentration has a linear relationship with the doping depth $N \propto t$, thus, we can conclude that the relationship between the plasma frequency of n-doped Si and the doping depth is given by

$$\omega_p \propto \sqrt{N} \propto \sqrt{t} \tag{7}$$

where t is the doping depth, and N is the doping concentration at the corresponding doping depth.

In our multilayer stacked structure model, the plasma frequency of n-doped Si in each layer is shown in Table 3. The previous work by S. Basu *et al.* [44] has demonstrated that the carrier mobility will gradually decrease with the doping concentration, and when the doping concentration reaches a relative high value ($> 1 \times 10^{19}$ cm^{-3}), the carrier mobility changes slightly with the doping concentration. In our multilayer model, as the doping concentration difference is small between layers, we can assume that the carrier mobility is constant in each layer, thus, the calculated collision frequency γ is fixed at 5×10^{13} rad/s. The calculated real and imaginary parts of the permittivity of doped-Si are shown in Figs. 7(b) and 7(c).

Based on the multilayer stacked structure model, the simulated absorption spectra of the fourth designed MBSSAEs with non-uniformly doped-silicon are shown in Fig. 7(d), and the values of the calculated average absorption/emissivity over the band of 3 μm – 5 μm, 8 μm – 14 μm, and 5 μm – 8 μm are 5.3%, 10.1%, and 64.1%, respectively. These results might contribute to the subsequent verification with experimental results.

In addition, our structure also performs a polarization-independent behavior (not shown here), which is due to the circular symmetry in the *x*-*y* plane. Therefore, the results show that the infrared spectral behaviors of our designed MBSSAE satisfy the requirements of the IR stealth.

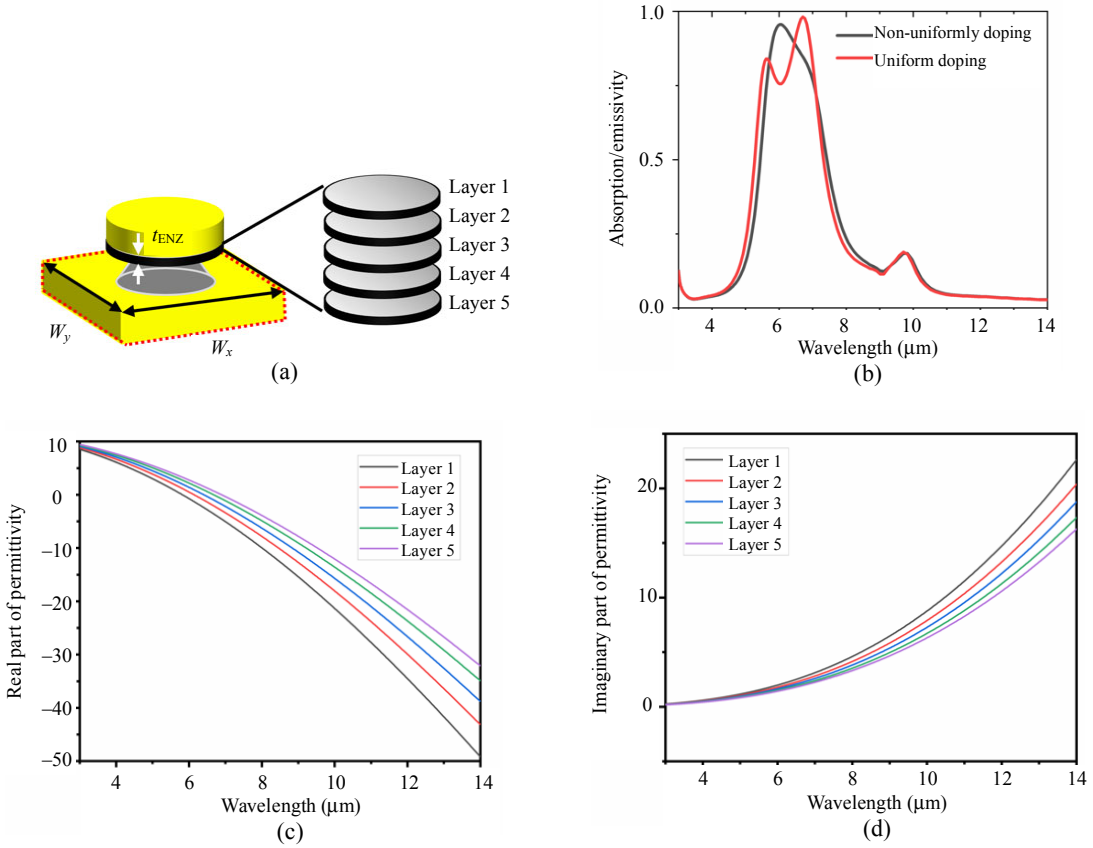

Fig. 7 Effect of non-uniform doping of the n-doped silicon layer: (a) schematic of the multilayer stacked structure model, the real (b) and imaginary (c) parts of the permittivity of doped silicon with five different doped concentrations as listed in Table 3, and (d) simulated spectra of the fourth designed MBSSAEs with uniformly doped-silicon (red solid line) and non-uniformly doped-silicon (black solid line).

Table 3 Multilayer model for the simulation of the carrier concentration inhomogeneity in highly-doped Si.

Layers	1	2	3	4	5
ω_p (rad/s)	1.12×10^{15}	1.063×10^{15}	1.02×10^{15}	0.98×10^{15}	0.95×10^{15}
γ (rad/s)	5×10^{13}	5×10^{13}	5×10^{13}	5×10^{13}	5×10^{13}

4. Conclusions

In conclusion, we have designed and investigated four kinds of MBSSAEs for the purpose of infrared stealth. And the fourth designed MBSSAE possesses the best infrared stealth performance, which has an optimized infrared suppression spectral characteristic in the IR transmission atmospheric window (3 μm – 5 μm and 8 μm – 14 μm) and an optimized radiative cooling spectral characteristic in the IR non-atmospheric window (5 μm – 8 μm). In this work, we have shown that the absorption bandwidth can be increased significantly through the introduction of an ENZ nanofilm. And we demonstrate characteristics of the tunable and polarization-independent absorption/ emission across the mid-infrared, which will also promote the implementation of high-performance sky radiative coolers. With a further acknowledge of the resonant mechanisms of the metamaterial-based absorber/ emitter, this work will provide an alternative approach for the narrow-band, dual-band, and even broadband perfect absorption, which has a promising potential for the application of spectrally selective thermal detection, optical sensor, thermophotovoltaic, radiative cooling, etc.

Acknowledgment

This work was supported by the National Natural Science Foundation of China (Grant Nos.

61734002, 61435010, 61177035, and 61421002).

References

[1] N. Lee, B. Yoon, T. Kim, J. Y. Bae, J. S. Lim, I. Chang, *et al.*, "Multiple resonance metamaterial emitter for deception of infrared emission with enhanced energy dissipation," *ACS Applied Materials & Interfaces*, 2020, 12(7): 8862–8869.

[2] X. Feng, X. Xie, M. Pu, X. Ma, Y. Guo, X. Li, *et al.*, "Hierarchical metamaterials for laser-infrared-microwave compatible stealth," *Optics Express*, 2020, 28(7): 9445–9453.

[3] K. Tang, X. Wang, K. Dong, Y. Li, J. Li, B. Sun, *et al.*, "A thermal radiation modulation platform by emissivity engineering with graded metal-insulator transition," *Advanced Materials*, 2020, 32(36): 1907071.

[4] N. Lee, T. Kim, J. S. Lim, I. Chang, and H. H. Cho, "Metamaterial-selective emitter for maximizing infrared stealth performance with energy dissipation," *ACS Applied Materials & Interfaces*, 2019, 11(23): 21250–21257.

[5] O. Salihoglu, H. B. Uzlu, O. Yakar, S. Aas, O. Balci, N. Kakenov, *et al.*, "Graphene-based adaptive thermal camouflage," *Nano Letters*, 2018, 18(7): 4541–4548.

[6] L. Zhao, H. Liu, Z. He, and S. Dong, "All-metal frequency-selective absorber/emitter for laser stealth and infrared stealth," *Applied Optics*, 2018, 57(8): 1757–1764.

[7] L. Xiao, H. Ma, J. Liu, W. Zhao, Y. Jia, Q. Zhao, *et al.*, "Fast adaptive thermal stealth based on flexible VO_2/Graphene/CNT thin films," *Nano Letters*, 2015, 15(12): 8365–8370.

[8] M. Y. Li, D. Q. Liu, H. F. Cheng, L. Peng, and M. Zu, "Manipulating metals for adaptive thermal camouflage," *Science Advances*, 2020, 6(22): eaba3494.

[9] J. J. Greffet, R. Carminati, K. Joulain, J. P. Mulet, S. Mainguy, and Y. Chen, "Coherent emission of light by thermal sources," *Nature*, 2002, 416(6876): 61–64.

[10] H. Chalabi, A. Alù, and M. L. Brongersma, "Focused thermal emission from a nanostructured SiC surface," *Physical Review B*, 2016, 94(9): 094307.

[11] S. Y. Lin, J. G. Fleming, E. Chow, J. Bur, K. K. Choi, and A. Goldberg, "Enhancement and suppression of thermal emission by a three-dimensional photonic crystal," *Physical Review B*, 2000, 62(4): R2243.

[12] C. Luo, A. Narayanaswamy, G. Chen, and J. Joannopoulos, "Thermal radiation from photonic crystals: a direct calculation," *Physical Review Letters*, 2004, 93(21): 213905.

[13] T. Inoue, M. De Zoysa, T. Asano, and S. Noda, "Realization of dynamic thermal emission control," *Nature Materials*, 2014, 13(10): 928–931.

[14] D. Costantini, A. Lefebvre, A. L. Coutrot, I. Moldovan Doyen, J. P. Hugonin, S. Boutami, *et al.*, "Plasmonic metasurface for directional and frequency-selective thermal emission," *Physical Review Applied*, 2015, 4(1): 014023.

[15] X. Liu, T. Tyler, T. Starr, A. F. Starr, N. M. Jokerst, and W. J. Padilla, "Taming the blackbody with infrared metamaterials as selective thermal emitters," *Physical Review Letters*, 2011, 107(4): 045901.

[16] D. G. Baranov, Y. Xiao, I. A. Nechepurenko, A. Krasnok, A. Alù, and M. A. Kats, "Nanophotonic engineering of far-field thermal emitters," *Nature Materials*, 2019, 18(9): 920–930.

[17] J. P. Nong, L. L. Tang, G. L. Lan, P. Luo, Z. C. Li, D. P. Huang, *et al.*, "Enhanced graphene plasmonic mode energy for highly sensitive molecular fingerprint retrieval," *Laser & Photonics Reviews*, 2021, 15(1): 2000300.

[18] J. P. Nong, L. L. Tang, G. L. Lan, P. Luo, Z. C. Li, D. P. Huang, *et al.*, "Combined visible plasmons of Ag nanoparticles and infrared plasmons of graphene nanoribbons for high-performance surface-enhanced Raman and infrared spectroscopies," *Small*, 2021, 17(1): 2004640.

[19] P. Luo, W. Wei, G. Lan, X. Wei, L. Meng, Y. Liu, *et al.*, "Dynamical manipulation of a dual-polarization plasmon-induced transparency employing an anisotropic graphene-black phosphorus heterostructure," *Optics Express*, 2021, 29(19): 29690–29703.

[20] K. K. Du, Q. Li, Y. B. Lyu, J. C. Ding, Y. Lu, Z. Y. Cheng, *et al.*, "Control over emissivity of zero-static-power thermal emitters based on phase-changing material GST," *Light: Science Applications*, 2017, 6(1): e16194.

[21] W. Streyer, S. Law, G. Rooney, T. Jacobs, and D. Wasserman, "Strong absorption and selective emission from engineered metals with dielectric coatings," *Optics Express*, 2013, 21(7): 9113–9122.

[22] T. Kim, J. Y. Bae, N. Lee, and H. H. Cho, "Hierarchical metamaterials for multispectral stealth of infrared and microwaves," *Advanced Function Materials*, 2019, 29(10): 1807319.

[23] L. Peng, D. Q. Liu, H. F. Cheng, S. Zhou, and M. Zu, "A multilayer film based selective thermal emitter

for infrared stealth technology," *Advanced Optical Materials*, 2018, 6(23): 1801006.

[24] M. Pan, Y. Huang, Q. Li, H. Luo, H. Zhu, S. Kaur, *et al.*, "Multi-band middle-infrared-compatible stealth with thermal management via simple photonic structures," *Nano Energy*, 2020, 69: 104449.

[25] N. Fang, H. Lee, C. Sun, and X. Zhang, "Sub-diffraction-limited optical imaging with a silver superlens," *Science*, 2005, 308(5721): 534–537.

[26] X. Ni, Z. J. Wong, M. Mrejen, Y. Wang, and X. Zhang, "An ultrathin invisibility skin cloak for visible light," *Science*, 2015, 349(6254): 1310–1314.

[27] N. I. Landy, S. Sajuyigbe, J. J. Mock, D. R. Smith, and W. J. Padilla, "Perfect metamaterial absorber," *Physical Review Letters*, 2008, 100(20): 207402.

[28] J. Hao, L. Zhou, and M. Qiu, "Nearly total absorption of light and heat generation by plasmonic metamaterials," *Physical Review B*, 2011, 83(16): 165107.

[29] X. Liu, T. Starr, A. F. Starr, and W. J. Padilla, "Infrared spatial and frequency selective metamaterial with near-unity absorbance," *Physical Review Letters*, 2010, 104(20): 207403.

[30] N. Liu, M. Mesch, T. Weiss, M. Hentschel, and H. Giessen, "Infrared perfect absorber and its application as plasmonic sensor," *Nano Letters*, 2010, 10(7): 2342–2348.

[31] J. A. Mason, S. Smith, and D. Wasserman, "Strong absorption and selective thermal emission from a midinfrared metamaterial," *Applied Physics Letters*, 2011, 98(24): 241105.

[32] A. Tittl, A. K. U. Michel, M. Schäferling, X. H. Yin, B. Gholipour, L. Cui, *et al.*, "A switchable mid-infrared plasmonic perfect absorber with multispectral thermal imaging capability," *Advanced Materials*, 2015, 27(31): 4597–4603.

[33] I. Puscasu and W. L. Schaich, "Narrow-band, tunable infrared emission from arrays of microstrip patches," *Applied Physics Letters*, 2008, 92(23): 233102.

[34] G. Ok, H. Youn, M. K. Kwak, K. Lee, Y. J. Shin, L. J. Guo, *et al.*, "Continuous and scalable fabrication of flexible metamaterial films via roll-to-roll nanoimprint process for broadband plasmonic infrared filters," *Applied Physics Letters*, 2012, 101(22): 223102.

[35] J. R. Hendrickson, S. Vangala, C. Dass, R. Gibson, J. Goldsmith, K. Leedy, *et al.*, "Coupling of epsilon-near-zero mode to gap plasmon mode for flat-top wideband perfect light absorption," *ACS Photonics*, 2018, 5 (3): 776–781.

[36] Y. Li, P. Zhang, Y. Liu, R. Jiang, Y. Gong, L. Deng, *et al.*, "Infrared epsilon-near-zero absorption excited by magnetic dipole resonance," *Optics Communications*, 2020, 472: 126015.

[37] Lumerical Solutions, Inc. http://www.lumerical.com/tcad-products/fdtd/.

[38] E. D. Palik, *Handbook of optical constants of solids*. San Diego: Academic Press, 1998.

[39] A. D. Rakić, A. B. Djurišic, J. M. Elazar, and M. L. Majewski, "Optical properties of metallic films for vertical-cavity optoelectronic devices," *Appli*ed *Optics*, 1998, 37(22): 5271–5283.

[40] G. Kirchhoff, "On the relation between the radiating and the absorbing powers of different bodies for light and heat," *The London, Edinburgh, and Dublin Philosophical Magazine and Journal of Science,* 1860, 20: 1–21.

[41] J. Park, J. H. Kang, X. Liu, and M. L. Brongersma, "Electrically tunable epsilon-near-zero (ENZ) metafilm absorbers," *Scientific Reports*, 2015, 5(1): 1–9.

[42] Y. B. Chen and F. C. Chiu, "Trapping mid-infrared rays in a lossy film with the Berreman mode, epsilon near zero mode, and magnetic polaritons," *Optics Express*, 2013, 21(18): 20771–20785.

[43] D. Yoo, F. de León-Pérez, M. Pelton, I. H. Lee, D. A. Mohr, M. B. Raschke, *et al.*, "Ultrastrong plasmon-phonon coupling via epsilon-near-zero nanocavities," *Nature Photonics*, 2021, 15(2): 125–130.

[44] S. Basu, B. J. Lee, and Z. M. Zhang, "Infrared radiative properties of heavily doped silicon at room temperature," *ASME Journal of Heat Transfer*, 2010, 132(2): 023301.